Submitted to *International Journal of Heat and Mass Transfer*, July 17, 2022; Revised January 22, 2023

A numerical study of the spectral radiative properties of packed bed with mixed bauxite and silica spheres

Chuyang Chen, Devesh Ranjan, Peter G. Loutzenhiser and Zhuomin M. Zhang*

George W. Woodruff School of Mechanical Engineering, Georgia Institute of Technology, Atlanta, Georgia 30332, USA

Bauxite and silica particles have gained increasing attention for applications in the field of concentrated solar power. In this work, a Monte Carlo ray-tracing simulation is performed to predict the radiative properties (absorptance, reflectance, and transmittance) of packed beds with mixed bauxite and silica spherical particles at wavelengths of 0.5, 2.6, 9.0, and 9.35 μm. These wavelengths are representative for the visible, near-infrared, and the mid-infrared regions that are important for solar and thermal radiation, respectively. A repeating unit-column approach is used to mathematically represent the particle bed. The effects of particle mixing ratio, volume fraction, and wavelength on the predicted radiative properties are examined. The obtained radiative properties are inputted to an inverse method to retrieve the effective absorption and scattering coefficients as well as the scattering albedo, which may be later used in a continuous-scale radiative heat transfer analysis. Furthermore, the independent scattering model is used to obtain the absorption coefficient and scattering albedo based on the absorption and scattering cross sections predicted by a Monte Carlo algorithm for a single particle. It is shown that the independent scattering model underpredicts the scattering coefficient for opaque particles but overpredicts the scattering coefficient for semitransparent particles for sufficiently high particle volume fractions. The radiative properties calculated from the independent scattering model are compared to the full Monte Carlo simulation of the particle bed to examine the influence of particle mixing on dependent scattering.

Keywords: Monte Carlo method, packed bed, particle mixture, radiative properties, scattering

* Corresponding author: zhuomin.zhang@me.gatech.edu

1. Introduction

The absorption and scattering mechanisms associated with the radiative heat transfer process in particulate or dispersed media differ from those in continuous or homogeneous media [1–5]. Due to the difference in refractive indices of the solid particles and the liquid/gaseous hosting medium, propagating lights or rays experience scattering at the phase boundaries [6–8]. The collective interactions promote additional attenuation, absorption, and scattering by the whole media, or the particle bed [9,10]. Recent experimental developments in the field of concentrated solar power (CSP) have motivated further investigation on the radiative heat transfer in particulate media [11–20]. Particles of hundreds of micrometers are used as the solar thermal energy storage (TES) media that forms granular flows for the absorption and storage of radiative energy and electricity production [21–29]. Due to computational complexity, multi-physics models incorporating conduction, convection, and radiation limit the modeling domain of the radiation as homogeneous media with simple geometries [30–35]. It is preferred to capture the radiative behaviors with simple parameters such as particle absorptance, and absorption and scattering coefficients in a gray-band or wide-band approximation. Nevertheless, it remains difficult to deduce these parameters given the complex configurations that particulate media may have, which include particle volume fraction, particle size, and mixing condition for dissimilar particles [36–40].

A number of studies have experimentally determined the radiative properties of individual particles and particulate media. Jeong et al. [41] obtained the average absorption and scattering cross sections of single particles by measuring the directional-hemispherical transmittance and reflectance of a layer of particles on a transparent tape. The scattering phase function is often obtained from angle-resolved light scattering measurements [41,42]. In the regime of independent

scattering, these properties have been used to estimate the effective absorption and scattering coefficients of the particulate media and consequently solve the representative radiative transfer equation on a continuous scale [43–46]. Without the information of angular scattering distribution, the effective absorption and scattering coefficients have been retrieved from the measured directional-hemispherical reflectance and transmittance [15]. In this case, the scattering is often assumed to be isotropic or based on an equivalent (*i.e.*, reduced) scattering coefficient. The continuous-scale modeling thus relies on the information of the effective absorption and scattering coefficients, and the phase function. However, once obtained, existing forward modeling methods including two-flux, three-flux, adding-doubling, discrete-ordinate, and continuous-scale Monte Carlo methods may be used to calculate the radiative properties [7–9,47]. The discrete-scale modeling for relatively large particles is usually associated with ray tracing based on geometric optics [48–50]. It directly models the radiative energy transport in the particulate media by numerically reconstructing the particle beds using representative spheres and model reflection and refraction at the interfaces [51–60]. The discrete-scale Monte Carlo simulation offers a relatively more robust method for exploring underling mechanisms of radiative heat transfer in particulate media with complex configurations, though challenges exist to account for realistic situations such as particle surface morphology and optical properties.

For complex configurations, such as polydispersion and particle mixing (different types), the radiative and other thermophysical properties could change from that of a monodispersed (*i.e.*, single type) particle bed. Christen et al. [61] showed that the effective thermal conductivity increases in a binomial particle system of bauxite ceramic particles, where the insertion of smaller sized particles in a particle bed results in the decrease of porosity. Chen et al. [40] developed a numerical model that incorporates polydispersion effects in modeling the spatial temperature

distribution of granular flows. Lipiński et al. [62] measured the transmittance of SiO_2-ZnO-C mixture at various mass ratios and thicknesses. By adding a small amount of the absorbing ZnO and C particles, the measured transmittance significantly decreases. Jäger et al. [63] used a continuous-scale Monte Carlo method to model the radiative properties of particle mixtures based on superposition of the individual contributions to the absorption and scattering coefficients. In atmospheric science, Petzold et al. [64] demonstrated that mixing of soot (carbon black) particles with mineral dust increases the aerosol optical thickness. Mishchenko and coworkers solved Maxwell's equation using the T-matrix method to study the effects of particle aggregation formed by mixing soot, dust, and sulfate particles on optical cross sections [65,66]. The full wave approach is computationally intensive, and the results are strongly affected by submicron particle sizes or separation distances. For relatively large sized particles, geometric optics approximation is the preferred choice for computational effectiveness [3,7,48]. There is a need for examining the spectral-dependent optical properties (*e.g.*, complex refractive index) and the mixing effect on the absorption and scattering mechanisms for particle beds [59,67].

A numerical study is carried out here to investigate the radiative properties of packed bed of mixed spherical solid particles at several discrete wavelengths from the visible to the mid-infrared. Bauxite and silica particles are chosen due to the increasing interest on their application in CSP applications. A discrete-scale Monte Carlo ray-tracing simulation is performed using repeating unit-column approach, which has been validated with previous works and with the full particle bed generation method. Absorption and scattering coefficients as well as scattering albedo for equivalent continuous media are retrieved from the simulated reflectance and transmittance using an inverse method. By performing ray-tracing calculation on a single particle and incorporating the superposition method, this work also develops an independent scattering model

for calculating the radiative properties based on the continuous-scale approach. Comparisons of the Monte Carlo simulation results with the independent scattering model shed light on the dependent scattering phenomenon with the presence of a particle mixture.

2. Numerical methods

This section briefly introduces the discrete-scale Monte Carlo method used in the present study for particle beds with different particle types of the same diameter. The simulated radiative properties (T and R) are used in an inverse method to extract the absorption and scattering coefficients of the particulate medium as functions of the volume fraction and mixing ratio. This allows a quantitative comparison with those predicted by the independent scattering theory to examine the conditions when dependent scattering becomes important. The procedures of obtaining the absorption and scattering coefficients using either the inverse method or from the independent scattering theory are also described.

2.1. Monte Carlo ray-tracing simulation

Modeling radiative transfer in particle beds in the geometric-optics regime based on the Monte Carlo method includes a numerical representation of spatial coordinates of the particles and tracing the rays or ray-bundles in a three-dimensional environment. The numerical representation of particles can be developed either by rigorous formulations based on established understanding of particle packing behavior [48,49,51–58] or using dedicated programs (e.g., LIGGGHTS) with specific particle-generating schemes [13,20,60,67]. While the latter has become more popular in modern studies since it avoids complex mathematical relations for spatially distributed particles, it often suffers from inefficient computing power and/or much longer rendering time.

In the present study, a numerical representation is implanted to locate the center point of the spherical particles with the same size but different types. The number density of the two types of particles is denoted by N_1 and N_2, respectively. The particle number density in the bed is then $N = N_1 + N_2$. The mixing ratio is based on the number of type 1 particles to the total number of particles such that $r = N_1 / N$. In the present study, type 1 refers to silica and type 2 refers to bauxite particles.

The fundamental building block follows the face-centered cubic (FCC) structure, as shown in Fig. 1(a). FCC is chosen because it appears to be a more realistic configuration that allows a higher packing density without overlapping spheres [15,68]. Each of the six cubic cell corners contributes 1/8 of a particle to a given cell, and each of the cell face centers contributes 1/2 of a particle, thus amounting to four particles in a unit cell. Hence, the number of particles in each unit volume (*i.e.*, number density) is

$$N = \frac{4}{\xi^3} \tag{1}$$

where ξ is the length of each side of the unit cell. Each unit cell may be considered as two layers with a thickness of $\xi/2$ that contains two spheres within the unit cell. It can be shown that the particle volume fraction is

$$\phi_v = \frac{2\pi}{3}\left(\frac{d}{\xi}\right)^3 \tag{2}$$

where d is the diameter of the spherical particles for either type. For close-packing FCC spheres, ϕ_v reaches a maximum value of 0.74. For fixed d, increasing ξ results in reducing ϕ_v and N since $N = 6\phi_v / d^3$. The particle volume fraction for individual types is simply $r\phi_v$ for type 1 particles and $(1-r)\phi_v$ for type 2 particles. When the particle bed is not close-packing, a random number is

used for each layer to shift the particles in that layer laterally to create some randomization of the lateral positions for better representing the actual particle bed [15,48].

The particle bed may be generated layer by layer with sufficient lateral dimensions and specified thickness (or number of layers), as shown in Fig. 1(b). A random number is used to specify whether the particle is type 1 or type 2, illustrated by two different colors. Upon the incidence by a ray bundle, the corresponding material property (*e.g.*, refractive index) is invoked for calculating the reflection and refraction properties. The particle type and location information is stored for future calculations. This approach has an advantage that the particle bed only needs to be generated once and rays can be traced to determine the transmittance, reflectance, and absorptance of the bed. The disadvantage is that the lateral extension is very large and the exact location of the rays during the path must be determined. Hence, it requires a large computational memory as well as a longer computational time.

An alternative approach is based on periodic boundary conditions by stacking unit cells to form a unit column as shown in Fig. 1(c). Note that the z-direction is elongated in Figs. 1(b,c) for clarity. The lateral area of the unit column $\xi \times \xi$ defines the side walls. However, the particle center may be located outside the cell within a distance of $d/2$ from the side wall such that a portion of the spherical surface is inside the unit column. The particles are not assumed to have any material property until the interception of a bundle that triggers the generation of a random number χ. The property of the particle is then determined as either type 1 ($\chi < r$) or type 2 ($\chi > r$). Two horizontal planes, one above the top layer and one below the bottom layer of particles, defines the top and bottom surfaces of the particle bed virtually.

Both approaches are tested to give the same results and converge with sufficient number of ray bundles for either a single type of particles or a particle mixture. Additional validation was

done by comparison with the Monte Carlo simulation by González-Portillo et al. [59] for various particle bed volume fractions and optical properties of particles. The results show negligible differences. Comparison with experiments for densely packed beds of polycrystalline silica particles also provides evidence of the two approaches [15]. As expected, the unit-column approach is superior in terms of computational efficiency with significantly reduced time for convergence. Another advantage of the unit-column approach is that it avoids leakage of rays through the side boundaries of the generated layered structure. Due to limited computer memory, it is impossible to generate infinitely large number of particles in the lateral direction. The calculation of the interception location is also quite cumbersome in the layered generation approach. Throughout the rest of this work, only the unit-column approach is used and the ray-tracing algorithm is illustrated in the flow chart shown in Fig. 2 and explained in the following.

The starting point is to generate the particle bed with input parameters, including the sphere diameter d, volume fraction ϕ_v, and number of layers K. Note that ξ is determined by Eq. (2) and the thickness of the particle bed is $K\xi/2$. The particle mixing ratio r and the properties of each type of particles at the given wavelength are also prescribed. A ray bundle is launched from a location $\mathbf{s}=(s_x,s_y,s_z)$ above the unit column that is randomly distributed over the area $\xi\times\xi$ with a direction unit vector $\mathbf{v}=(v_x,v_y,v_z)$. For normal incidence, the initial direction unit vector is $\mathbf{v}=(0,0,1)$ since the positive z direction is downward as shown in Fig. 1(c). Air is treated as nonabsorbing. The ray bundle may intercept with the spherical surfaces within the unit volume or boundaries. If it intercepts with the side walls, periodic boundary condition is invoked. If at some stage the ray intercepts with the top or bottom boundaries, it will be counted as reflected or transmitted, respectively, since there is no reflection at these virtual surfaces.

Once the ray intercepts with a spherical surface, the type of particle needs to be determined to get the proper properties. While the surface reflection may be treated as diffuse, specular, or somewhere in between with a specularity parameter [15], the surfaces are assumed to be specular in the present study since the focus is on the effect of particle mixture. Since the code includes a secularity parameter, non-specular surfaces may be considered in the future to better represent the real situations. For determination of whether the ray is reflected or refracted, a random number is generated and compared to the surface reflectance calculated based on Fresnel's coefficients [68]. If reflected, the ray is continuously traced until it intercepts with another sphere or boundary of the unit column. If the ray enters the particle by refraction, it is assumed that the particle is made of a homogeneous or effectively homogeneous material such that no scattering occurs inside the particle. If the particle is highly absorbing, it may be treated as opaque so that the ray bundle is either absorbed or reflected. For semitransparent particles, the propagation step size δ is calculated by

$$\delta = \frac{\lambda}{4\pi\kappa}\ln(\chi) \tag{3}$$

where λ is the wavelength in vacuum, κ is the absorption index or imaginary part of the complex refractive index $\tilde{i}$, and χ is a random number. If the distance to the next interception location greater than δ, the ray is considered absorbed. Otherwise, the ray reaches the next interception on spherical surface. If refracted, it goes to the air and is further traced. If the ray is reflected, it is still inside the particle. Then, δ is reduced by the interception distance and traced to the next interception. In the case when the incidence angle for a ray from air is close to 90°, the refraction angle is near the critical angle. If the ray is not absorbed, the reflectivity for incident from the medium to air is very close to 1. Since δ is very large for the medium with very low absorption index, the ray may experience numerous reflections inside the sphere. To circumvent

this difficulty, only a limiting number of reflections (say 10^5) is allowed; afterward, the ray will be counted as being absorbed and a new incident ray bundle will be launched.

The ratio of the transmitted and reflected ray bundles to the total number of ray bundles yields (directional–hemispherical) transmittance and reflectance (T and R), respectively, and the absorptance is calculated by $\alpha = 1 - T - R$. The total number of photon bundles used in each run is typically 10^5. It takes 10 runs to obtain the average and standard deviation so that the statistical variation can be assessed to ensure the computational accuracy. Hence, the final simulation result is based on the average of 10^6 bundles. In the semitransparent spectral region, it takes a much longer time to perform the ray tracing for each ray bundle. Therefore, the total number of bundles is reduced to improve the calculation speed without significantly reducing the computational accuracy.

2.2. Forward and inverse adding-doubling methods

The Monte Carlo ray tracing described previously is a discrete-scale simulation that treats the dispersed particle bed as an inhomogeneous medium. It is often desired to model the particle bed as a homogeneous medium to perform energy balance on an infinitesimal control volume to describe the absorption, scattering, and propagation of a ray pencil or intensity [7,8]. For a participating medium, the radiative transfer equation (RTE) is generally applicable using wavelength-dependent absorption coefficient a_λ and scattering coefficient $\sigma_{\lambda,\text{true}}$, along with a suitable scattering phase function. The actual phase function is very complicated and often not known. For anisotropic scattering, the Henyey–Greenstein (HG) phase function allows the distinction of the forward and backward scattering with an asymmetric factor (g) [8,9,41]. The calculated hemispherical radiative properties based on the HG phase function may be

approximated using isotropic scattering by replacing the "true" scattering coefficient to a reduced scattering coefficient as follows: $\sigma_\lambda = (1-g)\sigma_{\lambda,\text{true}}$. In reality, the phase function is very complicated, especially for semitransparent and irregular particles [41,69].

The (forward) adding-doubling method is convenient for calculating the directional–hemispherical reflectance and transmittance of a layered structure if each layer can be treated as a homogeneous medium. Furthermore, the inverse solution allows the extraction of the radiative properties from the known values of T and R [47]. The inverse adding-doubling (IAD) method was previously applied to extract a_λ and σ_λ based on experimentally measured R and T [15]. In the present study, IAD is applied to the simulated radiative properties T and R for the given bed thickness to obtain the a_λ and σ_λ, by assuming that the refractive index of the medium is the same as air to avoid boundary reflection and the scattering is isotropic ($g = 0$) so that $\sigma_\lambda = \sigma_{\lambda,\text{true}}$. The scattering albedo is defined as $\omega_\lambda = \sigma_\lambda / (a_\lambda + \sigma_\lambda)$. The absorption coefficient and scattering albedo are key input parameters to the radiative heat transfer analysis between the particle bed medium and the walls under various irradiation conditions [26,29].

2.3. Independent scattering model

For a plane wave passing through a single particle, the absorption and scattering cross sections may be determined based on physical optics (electromagnetic waves) or geometric optics [6,7]. When the diameter of the particles or the distance between the particles or particle clusters are comparable with the wavelength of interest, interference and evanescent waves may occur to introduce dependent scattering effect [2-4,70,71]. In the present study, the considered spherical diameter and separation distance are much larger than the wavelength. From the geometric-optics point of view, the scattering phenomenon is due to multiple reflections and refractions that change

the ray direction. Nevertheless, the independent scattering theory may not be able to accurately predict the absorption and scattering coefficients of the particulate medium, due to geometric multiple scattering in an elementary volume [5,43,44,48,49,51-53]. In order to make a comparison between the inversely obtained absorption and scattering coefficients with those by assuming independent scattering as discussed next.

If the scattering events are assumed independent of each other, the cross sections are determined by summing the absorption and (reduced) scattering coefficients as [3,7,15]

$$a_\lambda = NC_{\text{abs}} \tag{4}$$

$$\sigma_\lambda = (1-g)NC_{\text{sca}} \tag{5}$$

where C_{abs} and C_{sca} are the particle absorption and scattering cross sections at the given wavelength, though subscript λ is omitted for simplicity. Equations (4) and (5) are for a single type of particles in the packed bed. For a particle mixture with two types of particles of the same size, the mean absorption coefficient and (reduced) scattering coefficient may be obtained by

$$a_\lambda = rNC_{\text{abs},1} + (1-r)NC_{\text{abs},2} \tag{6}$$

$$\sigma_\lambda = (1-g_1)rNC_{\text{sca},1} + (1-g_2)(1-r)NC_{\text{sca},2} \tag{7}$$

where subscripts 1 and 2 are used to denote the two types of particles.

To predict the absorption and scattering coefficient, the scattering cross sections are directly calculated using a Monte Carlo algorithm for single particle of each type [15,41]. The algorithm also gives the scattering phase function. The procedure is to fit it to the HG function with an asymmetry factor g. The absorption and (reduced) scattering coefficient calculated from Eqs. (6) and (7) are used with the adding-doubling method to calculate the radiative properties of a particle bed with specified thickness. The results from the independent scattering model are

compared with the Monte Carlo simulation of the particle bed to investigate when dependent scattering may become significant and should be considered.

3. Results and discussion

The refractive index and absorption index of silica and bauxite are plotted in Fig. 3. The data for (crystalline) silica (α-SiO_2) are mainly taken from Refs. [72,73] with some modifications done by Chen et al. [15] for the absorption index in the short wavelength region to account for impurities. The dielectric function of bauxite is modeled with effective medium theory considering the individual dielectric functions and volume fractions of the metal oxides and pore [14]. Then the complex refractive index is calculated from the effective dielectric function of bauxite with the specified composition for the Carbobead HSP particles [13,14]. It is assumed that the particles are homogeneous without internal scattering. The radiative properties of particles are sensitive to the spectral dependent optical constants. Four representative wavelengths are selected from the visible to the mid-infrared. The radiation penetration depth (or photon mean free path) ℓ $\pi\kappa$) is an important parameter as seen in Eq. (3). If $d >> \ell$, the particle may be treated as opaque. In the present study, the particle diameter d is set at 200 μm, a typical value for CSP applications [13-15]. The normal reflectivity at air-particle interface is calculated by [68]

$$\rho_\lambda = \frac{(n-1)^2 + \kappa^2}{(n+1)^2 + \kappa^2} \tag{8}$$

While the actual reflectance depends on the incidence angle, ρ_λ is a good indication of the magnitude of surface reflection. The values of ℓ and ρ_λ for each material are listed in Table 1 together with the optical constants (n and κ) at the corresponding wavelength. Note that Fresnel's coefficients are always used in the Monte Carlo calculations.

The wavelength $\lambda = 0.5$ μm corresponds to the visible region and the main portion of the solar spectrum ($0.4\ \mu\text{m} < \lambda < 2\ \mu\text{m}$) where silica is highly transparent and bauxite is highly absorbing. The normal reflectivity at the interface is less than 0.1 for both materials. In the near infrared at $\lambda = 2.6$ μm, the optical properties of silica are similar to those at $\lambda = 0.5$ μm. However, the absorption index for bauxite particles is much smaller than at other wavelengths, resulting in ℓ μm such that the individual particle is semitransparent. Nevertheless, multiple reflections inside the particle and between particles in the bed tend to give rise to stronger absorption when the particle bed is compared with a homogeneous plate sample [15].

There are phonon resonances for both silica and bauxite in the mid-infrared. The wavelengths of 9.0 and 9.35 μm are located above and below the resonance wavelength for silica as seen from Figs. 3(a) and 3(b). At $\lambda = 9.0$ μm, $n < 1$ and $\kappa = 2.75$ for silica, resulting in a high surface reflectivity, which is typical metallic behavior [68]. For silica at $\lambda = 9.35$ μm, n reaches a peak of 7.21 and $\kappa \approx 3$; subsequently, the normal reflectivity is 0.62. At $\lambda = 9.0$ and 9.35 μm, both bauxite and silica particles are opaque. However, bauxite particles are highly absorbing with very small surface reflection, especially at $\lambda = 9.35$ μm.

There is a trade-off in terms of the thickness (or number of layers) of the particle bed and the particle volume fraction to be used in the simulation. After a large number of testing, it is decided to fix the number of layers $K = 15$ for all runs, while changing ϕ_v from 0.01 to 0.7. The particle bed thickness L varies between about 2 mm for high packing densities and 8 mm for low packing densities. The detailed results at different wavelengths are described in the subsections.

3.1 Monte Carlo simulation results for λ = 0.5 μm

The transmittance, reflectance, and absorptance at $\lambda = 0.5$ μm for various mixing ratio are shown in Fig. 4(a-c) as functions of the particle volume fraction. Since bauxite particles are opaque and highly absorbing, increasing *r* or the silica content results in reduced absorptance but increased reflectance and transmittance. It appears that the radiative properties are more sensitive when a small portion of silica particles are replaced by bauxite particles than the reverse scenario. For example, when *r* changes from 1 to 0.9, the absorptance is nearly doubled and the reflectance significantly decreases. Hence, the increment of *r* is intentionally chosen uneven to ensure that the curves are not too crowded for small *r* values.

For $r = 0$ (pure bauxite particles), $T < 0.01$ at $\phi_v > 0.15$ and $T < 0.001$ at $\phi_v = 0.24$. While Fig. 4(a) does not provide sufficient resolution for $T < 0.005$, calculated results are reliable until $T < 2\times10^{-5}$. For $r = 0$ and 0.1, the transmittance decreases as ϕ_v increases; furthermore, $\alpha \approx 1 - R$ for $\phi_v > 0.3$ since the transmittance is negligibly small. Further increase ϕ_v results in a slightly increased *R* and subsequently reduced α.

For large *r* values, say 0.9 and 1, the radiative properties do not change monotonically with ϕ_v. For $\phi_v < 0.3$, *T* decreases and *R* increases with increasing ϕ_v until reaching a valley and plateau, respectively. Further increasing of ϕ_v leads to a slight increase in *T* and reduction in *R*. This may be explained by forward scattering ($g > 0$) due to multiple reflections/refractions for lightly absorbed particles [41]. For small values of ϕ_v, blockage and additional scattering events cause an increase in *R* and a reduction *T* as ϕ_v increases. However, when ϕ_v is further increased, the forward scattering effect gives rise to a higher *T* and smaller *R*. Due to the competing effect between *T* and *R*, α does not change much when $\phi_v > 0.4$.

The absorption coefficient, scattering coefficient, and scattering albedo retrieved using IAD based on the radiative properties shown in Fig. 4 are plotted in Fig. 5(a-c). It is seen that a_λ decreases by a factor of 25-30 as r changes from 0 to 1. The wavy feature for $r = 0$ is due to the uncertainty in IAD with a very low transmittance ($T < 0.001$). With respect to the scattering coefficient, for $\phi_v < 0.4$, σ_λ increases with both r and ϕ_v. For $0.4 < \phi_v < 0.7$, σ_λ for the bed of opaque particles ($r = 0$) continues to increase with increasing ϕ_v, while a slightly decreasing trend is observed for the bed with semitransparent particles ($r = 1$). Consequently, several crossovers occur in the σ_λ curves with different r, suggesting that dependent scattering becomes important. Interestingly, σ_λ is the largest for $r = 0.9$ when $\phi_v > 0.52$.

When $\omega_\lambda = 0.5$, the absorption and scattering coefficients are the same. This roughly corresponding to $r = 0.8$ as shown in Fig. 5(c). When $r = 1$, $\omega_\lambda \approx 0.9$ so that σ_λ is an order of magnitude higher than a_λ. When $r = 0$, the ω_λ increases from approximately 0.1 to 0.2, when ϕ_v changes from 0.01 to 0.7, suggesting that the scattering coefficient increases with the volume fraction of particles faster than the absorption coefficient.

It is instructive to compare two cases: (i) $\phi_v = 0.07$ and $r = 0$ and (ii) $\phi_v = 0.7$ and $r = 0.9$. Case (i) corresponds to pure bauxite particles, while case (ii) corresponds to a mixture with the same volume fraction of bauxite particles since $\phi_{v,\text{bauxite}} = \phi_v(1-r)$, but with additional silica particles. The radiative properties are $\alpha = 0.9$ and $R = 0.02$ for case (i), and $\alpha = 0.7$ and $R = 0.2$ for case (ii). The comparison of the two cases shows that for the same volume fraction of bauxite particles, a dense particle bed with mixing ($r = 0.9$, $\phi_v = 0.7$) produces lower absorptance and much higher reflectance than the dilute particle bed of pure bauxite particles ($r = 0$, $\phi_v = 0.07$). When comparing the absorption and scattering coefficients of these two cases using Fig. 5(a,b), it

can be seen that a_λ is slightly lower (by 15%) while σ_λ is much higher (by 16 times) for case (ii) the particle mixture than for case (i) the bauxite bed. Adding silica particles to the bauxite particle bed results in increased scattering coefficient but does not change the absorption coefficient very much. One may also compare case (ii) with the situation of pure silica ($r = 1$) at $\phi_v = 0.63$. Adding 10% bauxite particles to the pure silica bed yields a rapid increase in α (from 0.38 to 0.70) and decrease in R (from 0.35 to 0.20). Furthermore, a_λ increases by a factor of 3.4 while σ_λ does not change significantly.

3.2 Prediction by the independent scattering model for λ = 0.5 μm

As discussed in Section 2.3, the absorption and scattering coefficients may be directly calculated by superposing the contributions by individual particles. The absorption and scattering efficiency factors are the normalized absorption and scattering cross sections such that

$$Q_{\text{abs}} = C_{\text{abs}} / (\pi d^2 / 4) \tag{9}$$

and

$$Q_{\text{sca}} = C_{\text{sca}} / (\pi d^2 / 4) \tag{10}$$

They are calculated with a Monte Carlo algorithm for a single particle of each type using the known optical constants, along with the asymmetry factor g that is fitted to the numerically obtained phase function [15,41]. Table 2 lists the calculated Q_{abs}, Q_{sca}, and g at all four wavelengths. These values are plugged into Eqs. (6) and (7) to obtain the absorption and scattering coefficients. Then the forward adding-doubling method is used to calculate the radiative properties. Note that $Q_{\text{abs}} + Q_{\text{sca}} = 1$ since the incident photons are either absorbed or scattered by the particle.

At $\lambda = 0.5$ μm, both bauxite and silica particles are forward scattering ($g > 0$) even though the bauxite particle is opaque and the silica particle is semitransparent or slightly absorbing. The

results for a_λ and ω_λ calculated from the independent scattering model (indicated in the figure as "Ind. Scat. Model" and represented by the circles) are compared with those obtained from Monte Carlo simulation (curves) as shown in Fig. 6. When the diameter of the particle is fixed, the number density is proportional to the particle volume fraction. Hence, for a given r, both a_λ and σ_λ are proportional to ϕ_v; consequently, ω_λ versus ϕ_v relations are flat lines. The r values in Fig. 6 are chosen to be 0, 0.4, 0.8, and 1 for clarity and simplicity.

The absorption coefficient calculated from both methods agrees well, with a deviation typically less than 30%. Relatively large difference by a factor of 2-3 exists in the predicted scattering coefficient. Although σ_λ is not shown in the figure, the difference between the two models is manifested by the difference in ω_λ. When r = 0, ω_λ predicted by the Monte Carlo simulation increases with ϕ_v due to dependent scattering. This is consistent with the previous scaling model suggested by Singh and Kaviany [49] for opaque particles. When r = 0.8 and 1.0, the Monte Carlo simulation yields a smaller ω_λ and therefore a smaller σ_λ than the independent scattering model. A crossover is observed at $\phi_v = 0.35$ in ω_λ obtained by the two methods for a mixing ratio r = 0.4. Overall, the deviation between the independent scattering model and the Monte Carlo simulation is less than 30%. The independent scattering model tends to overpredict the scattering coefficient for large r and underpredict the scattering coefficient for smaller r.

As shown in Fig. 7(a), the independent scattering model overpredicts R for r = 1 and failed to capture the trend of R when $\phi_v > 0.4$. When r = 0.4, it overpredicts R for $\phi_v < 0.28$ and then underpredicts R for $\phi_v > 0.28$, though the deviation is relatively small. When r = 0, the independent scattering model underpredicts R, especially for large ϕ_v, suggesting a stronger dependent scattering behavior as the interparticle distances become smaller. The absorptance comparison is

shown in Fig. 7(b). Again, the deviation is getting larger for large ϕ_v when $r = 0$ and 1. Due to the opposite trends in the deviation for opaque and semitransparent particles, the predicted α becomes closer when ϕ_v is larger for $r = 0.4$ and 0.8. As discussed in the work of Singh and Kaviany [49], it is not feasible to find a general scaling factor when dealing with semitransparent particles. The geometric multiple scattering becomes more complex with semitransparent particles.

3.3 Results for $\lambda = 2.6$ μm

At $\lambda = 2.6$ μm, both bauxite and silica particles are semitransparent with internal absorption. As shown in Table 1, the penetration depths are 808 μm and 29,600 μm for bauxite and silica, respectively. Both bauxite and silica particles are forward scattering, and it is interesting to note that $Q_{\text{sca}}(1-g)$ happen to be the same for the two types of particles according to Table 2.

In Fig. 8, the results obtained from the two methods for R, α, a_λ and ω_λ are plotted against ϕ_v for $r = 0$, 0.4, 0.8, and 1. The bauxite particles are more absorbing, resulting in a reduction in R and increase in α as r decreases as shown in Fig. 8(a,b). Because both types of particles are semitransparent, the independent scattering model tends to over predict R and gives a monotonically increasing trend for R as ϕ_v increases that deviates from the Monte Carlo simulation especially for large r and ϕ_v. The independent scattering model predicts α well for $\phi_v < 0.45$ and start to overpredict α as ϕ_v further increases. For $r = 0$ and 0.4, the independent scattering model predicts α well when ϕ_v is either small or large, but underpredicts α for $0.06 < \phi_v < 0.6$. Compared with $\lambda = 0.5$ μm the maximum absorptance ($r = 0$) is approximately 0.8. While not shown in Fig. 8, the transmittance is generally higher than that at $\lambda = 0.5$ μm for

the same r value. When $r = 0$, $T > 0.02$ from the Monte Carlo simulation even when $\phi_v = 0.7$, suggesting that the bed with 15 layers of bauxite particle is semitransparent.

As shown in Fig. 8(c), the agreement in a_λ between the two methods is reasonable though deviations start at $\phi_v > 0.55$, the values of a_λ at $\lambda = 2.6$ μm are much smaller than those for the corresponding r at $\lambda = 0.5$ μm as shown in Fig. 6(a). The independent scattering model overpredicts the scattering albedo as shown in Fig. 8(d), in which the ordinate axis starts at 0.5 since even $r = 0$, $\sigma_\lambda > a_\lambda$ at $\lambda = 2.6$ μm. This suggests that for semitransparent particles, dependent scattering causes a reduction in the scattering coefficient for all r values. The relative difference in ω_λ is typically 10% for $r = 0$ and 0.4, 5% for $r = 0.8$, and about 1% for $r = 1$, suggesting that in this case, the independent scattering model gives reasonable predictions of the absorption and scattering properties. Note that all the deviation from independent scattering model is due to geometric multiple scattering.

3.4 Results for λ = 9.0 μm and 9.35 μm

At $\lambda = 9.0$ and 9.35 μm, both silica and bauxite particles are essentially opaque since ℓ according to Table 1. The silica particle possesses a very high reflectivity at $\lambda = 9.0$ μm, resulting in a large Q_{sca} and small Q_{abs}. At $\lambda = 9.35$ μm for the silica particle, Q_{sca} is 50% greater than Q_{abs}. The bauxite particles are highly absorbing with a low reflectivity, resulting in a large Q_{abs} and small Q_{sca}, as shown in Table 2. Note that the bauxite particles are forward scattering, while the scattering by the silica particle is nearly isotropic according to the fitting to the HG phase function with $g = 0$ at $\lambda = 9.0$ μm and $g = -0.02$ at $\lambda = 9.35$ μm.

The reflectance, absorptance, absorption coefficient, and scattering coefficient obtained by both the independent scattering model and the Monte Carlo simulation are shown Fig. 9. It should be noted that for $r = 0$, T quickly reduces below 0.01 for $\phi_v = 0.15$ and 0.001 for $\phi_v = 0.24$. Even with $r = 1$, $T < 0.01$ when $\phi_v > 0.32$. The small transmittance makes the IAD solution unreliable when $\phi_v >\approx 0.55$. Hence, only results for $\phi_v \le 0.5$ are shown.

Dependent scattering starts to play a role even for very low ϕ_v values and becomes stronger as ϕ_v increases. This results in an increasing R in the Monte Carlo simulation that is not captured by the independent scattering model toward large ϕ_v. Note that α increases with increasing ϕ_v, reaches a peak, and then decreases, especially for $r > 0$. Again, α is relatively high for $r = 0$. Comparing the independent scattering model with the Monte Carlo simulation, it can be seen that the predicted trend in the absorption coefficient agrees well; however, the trend in the scattering albedo (or scattering coefficient) is very different. The Monte Carlo simulation reveals an increasing ω_λ as ϕ_v increases. Furthermore, for the same ϕ_v, when the bed contains more and more silica particles, a_λ decreases and ω_λ increases significantly as shown in Fig. 9(c,d). While not shown, σ_λ also increases with r as expected due to the large Q_{sca} of the silica particle. The relative difference in ω_λ for $\phi_v = 0.5$ between the independent scattering model and Monte Carlo simulation is 56%, 35%, 16% and 6% for $r = 0$, 0.4, 0.8, and 1, respectively.

The calculated results for $\lambda = 9.35$ μm are plotted in Fig. 10. The general trend in R and α are similar to the corresponding cases for $\lambda = 9.0$ μm. Due to the reduction of ρ_λ and Q_{sca} of silica at $\lambda = 9.35$ μm as compared with those at $\lambda = 9.0$ μm, R also reduces when comparing the corresponding cases in Fig. 10(a) to Fig. 9(a) for large r. Similarly, α at $\lambda = 9.35$ μm as shown in Fig. 10(b) is higher than that at $\lambda = 9.0$ μm for large r. As seen from Fig. 10(c), the independent

scattering model underpredicts a_λ for $\phi_v > 0.2$. As ϕ_v increases, the independent scattering model starts to overpredict a_λ at some ϕ_v values when $r > 0$. These results contradict to the previous scaling factor [48,49]. The present study shows an increasing scattering coefficient and albedo with increasing ϕ_v for opaque particles. The maximum relative deviation is when $r = 0$ and $\phi_v = 0.5$, the value of ω_λ calculated from the Monte Carlo simulation is 0.063, which is more than twice that predicted by the independent scattering model (0.030). One of the reasons is that the previous works [48,49] were based on the attenuation only without considering the effect of reflectance. Earlier, Kamiuto et al. [44] developed a correlation to model the extinction coefficient ($a_\lambda + \sigma_\lambda$) as a function ϕ_v, while assuming that the absorption coefficient is not affected by dependent scattering. From the cases studied in this work, especially at $\lambda = 9.0$ and 9.35 μm with $r = 0$ or 1 (pure bauxite or silica particle bed), it is clear that surface reflection has a significant effect on dependent scattering. The effects on both the absorption and scattering coefficients need to be separately considered. It is noted that the spatial correlation or clustering may further enhance dependent scattering as recently demonstrated by Li and Chandran [60] using Monte Carlo simulations.

4. Conclusions

Packed beds with a mixture of bauxite and silica particles are numerically modeled to investigate the radiative properties as a function of particle bed configurations such as the particle volume fraction and mixing ratio. Four representative wavelengths are chosen to represent the solar and thermal emission spectra. The Monte Carlo simulation demonstrates that the addition of bauxite particles into the silica particle bed significantly increases the absorptance while decreasing the transmittance. The radiative properties depend on the mixing ratio nonlinearly. As

the particle volume fraction increases, there often exists a maximum in the absorptance due to the competing effect of changes in the transmittance and reflectance and the location of the maximum depends on the mixing ratio. Comparison with the independent scattering model has revealed some unexpected features in the radiative properties that either have not been observed previously or contradict with the previous observations based on the attenuation method. In general, the absorption coefficient is less affected by dependent scattering. As the particle volume fraction increases, the independent scattering model underpredicts the scattering coefficient for opaque particles but overpredicts the scattering coefficient for semitransparent particles. Even for opaque particles of the same type, the impact of dependent scattering on the radiative properties varies with the surface reflectivity. This work helps understand the radiative properties of particle beds with a mixture of large particles for concentrated solar power and other relevant applications.

Conflicts of interest

The authors declare no conflicts of interest.

Acknowledgements

This work was supported by the U.S. Department of Energy's Office of Energy Efficiency and Renewable Energy (EERE) under Solar Energy Technologies Office (EE0008372). ZMZ would also like to thank the financial support from the National Science Foundation (CBET-2029892). The views expressed herein do not necessarily represent the views of the U.S. Department of Energy, National Science Foundation, or the United States Government.

Nomenclature

a_λ	=	absorption coefficient, m^{-1}
C_{abs}	=	(spectral) absorption cross section, m^2
C_{sca}	=	(spectral) scattering cross section, m^2
d	=	particle diameter, m
g	=	asymmetry factor
K	=	number of layers
L	=	particle bed thickness, m
ℓ	=	radiation penetration depth, m
N	=	particle number density, $1/m^3$
$\tilde{\imath}$	=	complex refractive index
n	=	real part of the refractive index
R	=	directional–hemispherical reflectance
$\mathbf{s}$	=	location vector of a photon bundle
T	=	directional–hemispherical transmittance
$\mathbf{v}$	=	direction vector of a photon bundle

Greek symbols

α	=	absorptance $(1 - R - T)$
δ	=	step size of a photon bundle, m
κ	=	imaginary part of the refractive index or absorption index
λ	=	wavelength, m
ξ	=	side length of a unit cell, m
ρ_λ	=	normal reflectivity
σ_λ	=	(isotropic or reduced) scattering coefficient, m^{-1}
$\sigma_{\lambda,true}$	=	(true) scattering coefficient, m^{-1}
ϕ_v	=	particle volume fraction
χ	=	uniformly distributed random number between 0 and 1
ω_λ	=	scattering albedo

References

[1] S.W. Churchill, G.C. Clark, C.M. Sliepcevich, Light-scattering by very dense monodispersions of latex particles, Discussions of the Faraday Society 30 (1960) 192–199.

[2] M.Q. Brewster, C. Tien, Radiative transfer in packed fluidized beds: dependent versus independent scattering, J. Heat Transfer 104 (1982) 573–579.

[3] B. Drolen, C. Tien, Independent and dependent scattering in packed-sphere systems, J. Thermophys. Heat Transfer, 1 (1987) 63–68.

[4] D. Baillis, J.-F. Sacadura, Thermal radiation properties of dispersed media: theoretical prediction and experimental characterization, J. Quant. Spectrosc. Radiat. Transfer 67 (5) (2000) 327–363.

[5] Q. Brewster, Volume scattering of radiation in packed beds of large, opaque spheres, J. Heat Transfer 126 (2004) 1048–1050.

[6] H. Van der Hulst, Light Scattering by Small Particles, John Wiley & Sons, Inc., New York, 1957.

[7] J.R. Howell, M.P. Menguc, K. Daun, R. Siegel, Thermal Radiation Heat Transfer, 7th ed. ed., CRC Press, Boca Raton, 2020.

[8] M.F. Modest, S. Mazumder, Radiative Heat Transfer, 4th ed., Academic Press/Elsvier, Amsterdam, 2021.

[9] L. Dombrovsky, D. Baillis, Thermal Radiation in Disperse System: An Engineering Approach, Begell House, New York, 2010.

[10] Y. Yamada, J. Cartigny, C. Tien, Radiative transfer with dependent scattering by particles: Part 2—experimental investigation, J. Heat Transfer 108 (1986) 614–618.

[11] C.K. Ho, A review of high-temperature particle receivers for concentrating solar power, Appl. Therm. Eng. 109B (2016) 958–969.

[12] C.K. Ho, J.M. Christian, D. Romano, J. Yellowhair, N. Siegel, L. Savoldi, R. Zanino, Characterization of particle flow in a free-falling solar particle receiver, J. Sol. Energy Eng. 139 (2017) 021011.

[13] M.V. Bagepalli, J.D. Yarrington, A.J. Schrader, Z.M. Zhang, D. Ranjan, P.G. Loutzenhiser, Measurement of flow properties coupled to experimental and numerical analyses of dense, granular flows for solar thermal energy storage, Sol. Energy 207 (2020) 77–90.

[14] C. Chen, C. Yang, D. Ranjan, G.P. Loutzenhiser, Z.M. Zhang, Spectral radiative properties of ceramic particles for concentrated solar thermal energy storageapplications, Int. J. Thermophys. 41 (2020) Paper 152.

[15] C. Chen, C. Yang, D. Ranjan, G.P. Loutzenhiser, Z.M. Zhang, Spectral radiative properties of polydispersed SiO_2 particle beds, J. Thermophys. Heat Transfer 36 (2022) 858–869.

[16] K.M. Chung, J. Zeng, S.R. Adapa, T. Feng, M.V. Bagepalli, P.G. Loutzenhiser, K.J. Albrecht, C.K. Ho, R. Chen, Measurement and Analysis of Thermal Conductivity of Ceramic Particle Beds for Solar Thermal Energy Storage, Sol. Energy Mater. Sol. Cells, 230 (2021) 111271.

[17] J. Chen, A. Riaz, M. Taheri, A. Kumar, J. Coventry, W. Lipiński, Optical and radiative characterisation of alumina–silica based ceramic materials for high-temperature solar thermal applications, J. Quant. Spectrosc. Radiat. Transfer 272 (2021) 107754.

[18] J. Chen, V.M. Wheeler, B. Liu, A. Kumar, J. Coventry, W. Lipiński, Optical characterisation of alumina–mullite materials for solar particle receiver applications, Sol. Energy Mater. Sol. Cells 230 (2021) 111170.

[19] J. Chen, J.F. Torres, S. Hosseini, A. Kumar, J. Coventry, W. Lipiński, High-temperature optical and radiative properties of alumina–silica-based ceramic materials for solar thermal applications, Sol. Energy Mater. Sol. Cells 242 (2022) 111710.

[20] E. Johnson, S. Hicdurmaz, R. Buck, B. Hoffschmidt, Beam radiation penetration in particle beds for heat transfer modeling of a centrifugal solar particle receiver, J. Quant. Spectrosc. Radiat. Transfer 295 (2023) 108403.

[21] A. Gil, M. Medrano, I. Martorell, A. Lázaro, P. Dolado, B. Zalba, L.F. Cabeza, State of the art on high temperature thermal energy storage for power generation. Part 1—Concepts, materials and modellization, Renew. Sustain. Energy Rev. 14 (2010) 31–55.

[22] D. Barlev, R. Vidu, P. Stroeve, Innovation in concentrated solar power, Sol. Energy Mater. Sol. Cells, 95 (2011) 2703–2725.

[23] Z. Ma, G. Glatzmaier, M. Mehos, Fluidized bed technology for concentrating solar power with thermal energy storage, J. Sol. Energy Eng. 136 (2014) 031014.

[24] N.P. Siegel, M.D. Gross, C.K. Ho, T. Phan, J. Yuan, Physical properties of solid particle thermal energy storage media for concentrating solar power applications, Energy Procedia, 49 (2014) 1015–1023.

[25] N.P. Siegel, M.D. Gross, R. Coury, The development of direct absorption and storage media for falling particle solar central receivers, J. Sol. Energy Eng. 137 (2015) 041003.

[26] C.K. Ho, Advances in central receivers for concentrating solar applications, Sol. Energy, 152 (2017) 38–56.

[27] M.T. Islam, N. Huda, A. Abdullah, R. Saidur, A comprehensive review of state-of-the-art concentrating solar power (CSP) technologies: Current status and research trends, Renew. Sustain. Energy Rev. 91 (2018) 987–1018.

[28] H. Al-Ansary, A. El-Leathy, S. Jeter, M. Golob, C. Nguyen, E. Djajadiwinata, S. Alaqel, R. Saeed, S. Abdel-Khalik, Z. Al-Suhaibani, Design features of the world's first commercial concentrating solar power plant using the particle heating receiver concept, in: Proc. ASME 2019 13th Int. Conf. Ener. Sust., Paper ES2019-3856.

[29] B.H. Mills, C.K. Ho, N.R. Schroeder, R. Shaeffer, H.F. Laubscher, K.J. Albrecht, Design evaluation of a next-generation high-temperature particle receiver for concentrating solar thermal applications, Energies, 15 (2022) Paper 1657.

[30] W. Lipiński, A. Z'Graggen, A. Steinfeld, Transient radiation heat transfer within a nongray nonisothermal absorbing-emitting-scattering suspension of reacting particles undergoing shrinkage, Numerical Heat Transfer B 47 (2005) 443–457.

[31] L.A. Dombrovsky, W. Lipiński, A. Steinfeld, A diffusion-based approximate model for radiation heat transfer in a solar thermochemical reactor, J. Quant. Spectrosc. Radiat. Transfer 103 (2007) 601–610.

[32] L.A. Dombrovsky, W. Lipiński, Transient temperature and thermal stress profiles in semi-transparent particles under high-flux irradiation, Int. J. Heat Mass Transfer 50 (2007) 2117–2123.

[33] S. Haussener, W. Lipiński, P. Wyss, A. Steinfeld, Tomography-based analysis of radiative transfer in reacting packed beds undergoing a solid-gas thermochemical transformation, J. Heat Transfer. 132 (2010) 061201.

[34] L.A. Dombrovsky, J.H. Randrianalisoa, W. Lipiński, D. Baillis, Approximate analytical solution to normal emittance of semi-transparent layer of an absorbing, scattering, and refracting medium, J. Quant. Spectrosc. Radiat. Transfer 112 (2011) 1987–1994.

[35] N.P. Siegel, C.K. Ho, S.S. Khalsa, G.J. Kolb, Development and evaluation of a prototype solid particle receiver: on-sun testing and model validation, J. Sol. Energy Eng. 132 (2010) 021008.

[36] K. Ganesan, J. Randrianalisoa, W. Lipiński, Effect of morphology on spectral radiative properties of three-dimensionally ordered macroporous ceria packed bed, J. Heat Transfer 135 (2013) 122701.

[37] S. Haussener, W. Lipiński, J. Petrasch, P. Wyss, A. Steinfeld, Tomographic characterization of a semitransparent-particle packed bed and determination of its thermal radiative properties, J. Heat Transfer 131 (2009) 072701.

[38] B. Wang, L. Li, F. Schäfer, J.J. Pottas, A. Kumar, V.M. Wheeler, W. Lipiński, Thermal reduction of iron–manganese oxide particles in a high-temperature packed-bed solar thermochemical reactor, Chem. Eng. J. 412, (2021) 128255.

[39] W. Wang, Y. Shuai, B.G. Lougou, B. Jiang, Thermal performance analysis of free-falling solar particle receiver and heat transfer modelling of multiple particles, Appl. Therm. Eng. 187 (2021) 116567.

[40] J. Chen, A. Kumar, J. Coventry, J.-S. Kim, W. Lipiński, Numerical modelling of radiative heat transfer in a polydispersion of ceramic particles under direct high-flux solar irradiation, J. Quant. Spectrosc. Radiat. Transfer 278 (2022) 108008.

[41] S.Y. Jeong, C. Chen, D. Ranjan, P.G. Loutzenhiser, Z.M. Zhang, Measurements of scattering and absorption properties of submillimeter bauxite and silica particles, J. Quant. Spectrosc. Radiat. Transfer 276 (2021) 107923.

[42] J. Griffin, K. Stahl, R. Pettit, Optical properties of solid particle receiver materials: I. Angular scattering and extinction characteristics of Norton Masterbeads®, Sol. Energy Mater. 14 (1986) 395–416.

[43] K. Kamiuto, Correlated radiative transfer in packed-sphere systems, J. Quant. Spectrosc. Radiat. Transfer 43 (1990) 39–43.

[44] K. Kamiuto, M. Iwamoto, M. Sato, T. Nishimura, Radiation-extinction coefficients of packed-sphere systems, J. Quant. Spectrosc. Radiat. Transfer 45 (1991) 93–96.

[45] L. Hespel, S. Mainguy, J.-J. Greffet, Radiative properties of scattering and absorbing dense media: theory and experimental study, J. Quant. Spectrosc. Radiat. Transfer 77 (2003) 193–210.

[46] T. Hendricks, J.R. Howell, Absorption/scattering coefficients and scattering phase functions in reticulated porous ceramics, J. Heat Transfer 118 (1996) 79–87.

[47] S.A. Prahl, M.J. van Gemert, A.J. Welch, Determining the optical properties of turbid media by using the adding–doubling method, Appl. Opt. 32 (1993) 559–568.

[48] B. Singh, M. Kaviany, Independent theory versus direct simulation of radiation heat transfer in packed beds, Int. J. Heat Mass Transfer 34 (1991) 2869–2882.

[49] B. Singh, M. Kaviany, Modelling radiative heat transfer in packed beds, Int. J. Heat Mass Transfer 35 (1992) 1397–1405.

[50] J. Petrasch, S. Haussener, and W. Lipiński, Discrete vs. continuum-scale simulation of radiative transfer in semitransparent two-phase media, J. Quant. Spectrosc. Radiat. Transfer 112 (2011) 1450–1459.

[51] R. Coquard, D. Baillis, Radiative characteristics of opaque spherical particles beds: a new method of prediction, J. Thermophys. Heat Transfer 18 (2004) 178–186.

[52] R. Coquard, D. Baillis, Radiative characteristics of beds of spheres containing an absorbing and scattering medium, J Thermophys. Heat Transfer 19 (2005) 226–234.

[53] R. Coquard, D. Baillis, Radiative characteristics of beds made of large spheres containing an absorbing and scattering medium, Int. J. Therm. Sci. 44 (2005) 926–932.

[54] J.H. Zhou, Y.W. Zhang, J.K. Chen, Numerical simulation of laser irradiation to a randomly packed bimodal powder bed, Int. J. Heat Mass Transfer 52 (2009) 3137–3146.

[55] C.A. Wang, L.X. Ma, J.Y. Tan, L.H. Liu, Study of radiative transfer in 1D densely packed bed layer containing absorbing–scattering spherical particles, Int. J. Heat Mass Transfer 102, (2016) 669–678.

[56] A.V. Gusarov, Radiative transfer, absorption, and reflection by metal powder beds in laser powder-bed processing, J. Quant. Spectrosc. Radiat. Transfer 257 (2020) 107366.

[57] O.B. Kovalev, A.V. Gusarov, V.V. Belyaev, Morphology of random packing of micro-particles and its effect on the absorption of laser radiation during selective melting of powders, Int. J. Eng. Sci. 157 (2020) 103378.

[58] H. Wu, N. Gui, X. Yang, J. Tu, S. Jiang, A matrix model of particle-scale radiative heat transfer in structured and randomly packed pebble bed, Int. J. Therm. Sci. 153 (2020) 106334.

[59] L.F. González-Portillo, R. Abbas, K. Albrecht, C. Ho, Analysis of optical properties in particle curtains, Sol. Energy 213 (2021) 211–224.

[60] B. Li, R. B. Chandran, Effects of spatial correlations in particulate media on dependent scattering and radiative transport, Int. J. Heat Mass Transfer 182 (2022) 121951.

[61] C.E. Christen, J. Gómez-Hernández, T.P. Otanicar, Bimodal particle distributions with increased thermal conductivity for solid particles as heat transfer media and storage materials, Int. J. Heat Mass Transfer 184 (2022) 122250.

[62] W. Lipiński, E. Guillot, G. Olalde, A. Steinfeld, Transmittance enhancement of packed-bed particulate media, Exp. Heat Transfer, 21 (2008) 73–82.

[63] K. Jäger, W. Lipiński, H.G. Katzgraber, A. Steinfeld, Determination of thermal radiative properties of packed-bed media containing a mixture of polydispersed particles, Int. J. Therm. Sci., 48 (2009) 1510–1516.

[64] A. Petzold, A. Veira, S. Mund, M. Esselborn, C. Kiemle, B. Weinzierl, T. Hamburger, G. Ehret, K. Lieke, K. Kandler, Mixing of mineral dust with urban pollution aerosol over Dakar (Senegal): impact on dust physico-chemical and radiative properties, Tellus B: Chem. Phys. Meteorology 63 (2011) 619–634.

[65] M.I. Mishchenko, L. Liu, L.D. Travis, A.A. Lacis, Scattering and radiative properties of semi-external versus external mixtures of different aerosol types, J. Quant. Spectrosc. Radiat. Transfer 88 (2004) 139–147.

[66] L. Liu, M.I. Mishchenko, Scattering and radiative properties of complex soot and soot-containing aggregate particles, J. Quant. Spectrosc. Radiat. Transfer 106 (2007) 262–273.

[67] J.D. Yarrington, M.V. Bagepalli, G. Pathikonda, A.J. Schrader, Z.M. Zhang, D. Ranjan, P.G. Loutzenhiser, Numerical analyses of high temperature dense, granular flows coupled to high temperature flow property measurements for solar thermal energy storage, Sol. Energy 213 (2021) 350–360.

[68] Z.M. Zhang, Nano/Microscale Heat Transfer, 2nd ed., Springer Nature, Switzerland AG, 2020.

[69] P. Coray, W. Lipiński, A. Steinfeld, Experimental and numerical determination of thermal radiative properties of ZnO particulate media, J. Heat Transfer 132 (2010) 012701.

[70] T. Galy, D. Huang, L. Pilon, Revisiting independent versus dependent scattering regimes in suspensions or aggregates of spherical particles, J. Quant. Spectrosc. Radiat. Transfer 246 (2020) 106924.

[71] B.X. Wang, C.Y. Zhao, The dependent scattering effect on radiative properties of micro/nanoscale discrete disordered media, Ann. Rev. Heat Transfer 23 (2020) 231–353.

[72] Philipp, H. R., "Silicon dioxide (SiO_2), type α (Crystalline)," in *Handbook of Optical Constants of Solids*, edited by E. D. Palik, Academic Press, San Diego, 1998, pp. 719–747.

[73] R. Kitamura, L. Pilon, M. Jonasz, Optical constants of silica glass from extreme ultraviolet to far infrared at near room temperature, Appl. Opt. 46 (2007) 8118–8133.

Table 1: Complex refractive indices, radiation penetration depth, and normal reflectivity of silica and bauxite at the selected wavelengths.

	λ (μm)	0.50	2.60	9.00	9.35
Silica (Type 1)	n	1.55	1.51	0.19	7.21
	κ	7.67×10^{-6}	7.00×10^{-6}	2.75×10^{0}	3.05×10^{0}
	ℓ	5.19×10^{3}	2.96×10^{4}	2.60×10^{-1}	2.44×10^{-1}
	$\rho_{\lambda,n}$	0.05	0.04	0.92	0.62
Bauxite (Type 2)	n	1.82	1.71	1.46	1.37
	κ	2.17×10^{-2}	2.56×10^{-4}	4.28×10^{-1}	5.43×10^{-2}
	ℓ	1.83×10^{0}	8.08×10^{2}	1.67×10^{0}	1.37×10^{1}
	$\rho_{\lambda,n}$	0.08	0.07	0.06	0.02

Table 2: Monte Carlo simulation results for a single particle (d = 200 μm): absorption efficiency factor, scattering efficiency factor, and asymmetry factor.

	λ (μm)	0.50	2.60	9.00	9.35
Silica (Type 1)	Q_{abs}	0.03	0.01	0.09	0.40
	Q_{sca}	0.97	0.99	0.91	0.60
	g	0.57	0.59	0	–0.02
Bauxite (Type 2)	Q_{abs}	0.86	0.20	0.88	0.93
	Q_{sca}	0.14	0.80	0.12	0.07
	g	0.46	0.50	0.50	0.61

Figure captions:

Fig. 1. Schematics of (a) a unit cell of a face-centered cubic (FCC) structure, (b) layers that form a particle bed, and (c) the unit-column representation. In the lower figures, the z-direction is elongated for illustration purpose.

Fig. 2. Flow chart of the Monte Carlo ray-tracing simulation in a particle bed with the unit-column representation (periodic boundary condition).

Fig. 3. Complex refractive index of silica (type 1) and bauxite (type 2): (a) real part; (b) imaginary part. The vertical lines indicate the four representative wavelengths chosen for the present study, *i.e.*, λ = 0.5, 2.6, 9.0, and 9.35 μm.

Fig. 4. Radiative properties of packed bed with bauxite and silica particles at λ = 0.5 μm obtained using the Monte Carlo simulation: (a) transmittance; (b) reflectance; (c) absorptance. The number of layers (K) is set as 15 for all simulations.

Fig. 5. IAD results for particle bed mixture at λ = 0.5 μm: (a) absorption coefficient; (b) scattering coefficient; (c) scattering albedo.

Fig. 6. Comparison of the independent scattering model with the Monte Carlo simulation for λ = 0.5 μm: (a) absorption coefficient; (b) scattering albedo.

Fig. 7. Comparison of the independent scattering model with the Monte Carlo simulation for λ = 0.5 μm: (a) reflectance; (b) absorptance.

Fig. 8. Comparison of the independent scattering model with the Monte Carlo simulation for λ = 2.6 μm: (a) reflectance; (b) absorptance; (c) absorption coefficient; (d) scattering albedo.

Fig. 9. Comparison of the independent scattering model with the Monte Carlo simulation for λ = 9.0 μm: (a) reflectance; (b) absorptance; (c) absorption coefficient; (d) scattering albedo.

Fig. 10. Comparison of the independent scattering model with the Monte Carlo simulation for λ = 9.35 μm: (a) reflectance; (b) absorptance; (c) absorption coefficient; (d) scattering albedo.

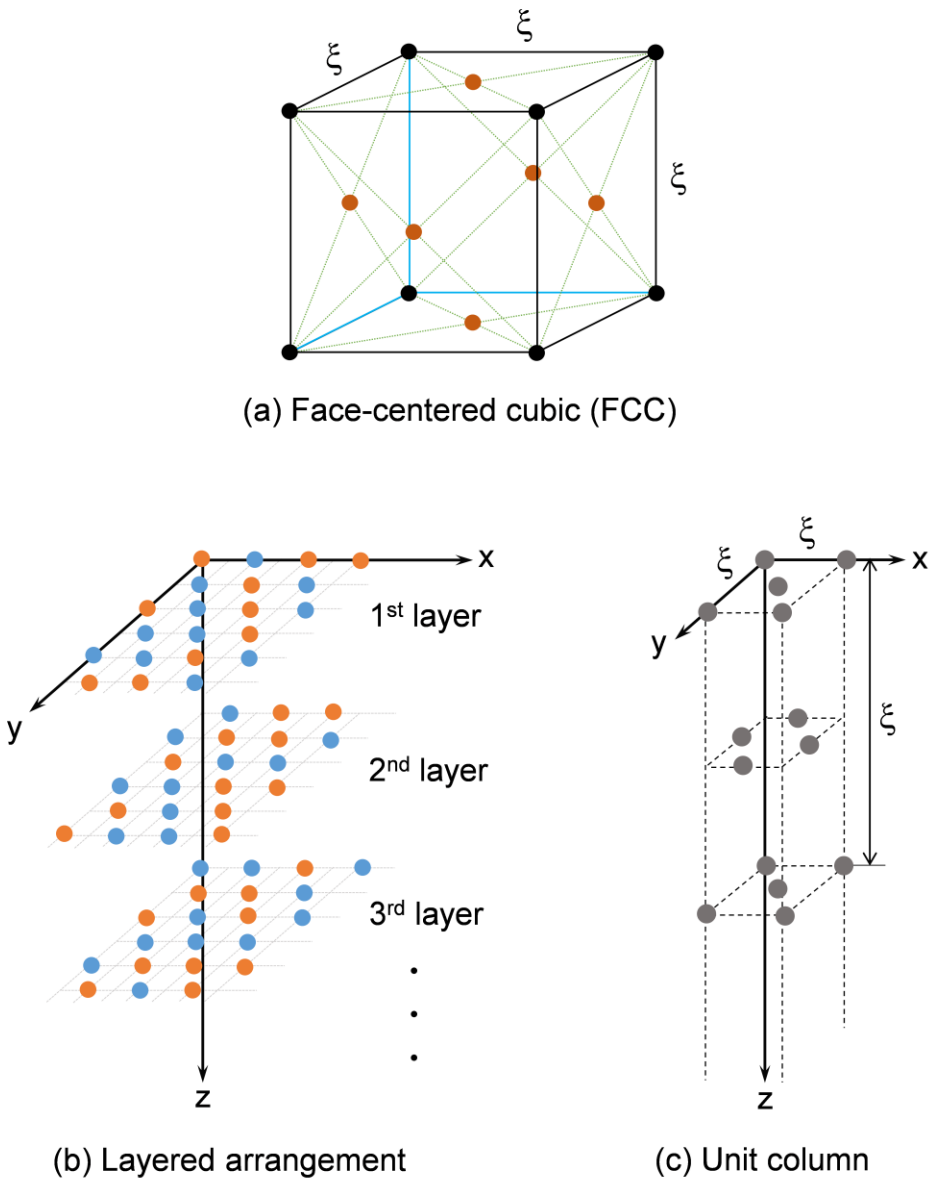

Fig. 1. Schematics of (a) a unit cell of a face-centered cubic (FCC) structure, (b) layers that form a particle bed, and (c) the unit-column representation. In the lower figures, the *z*-direction is elongated for illustration purpose.

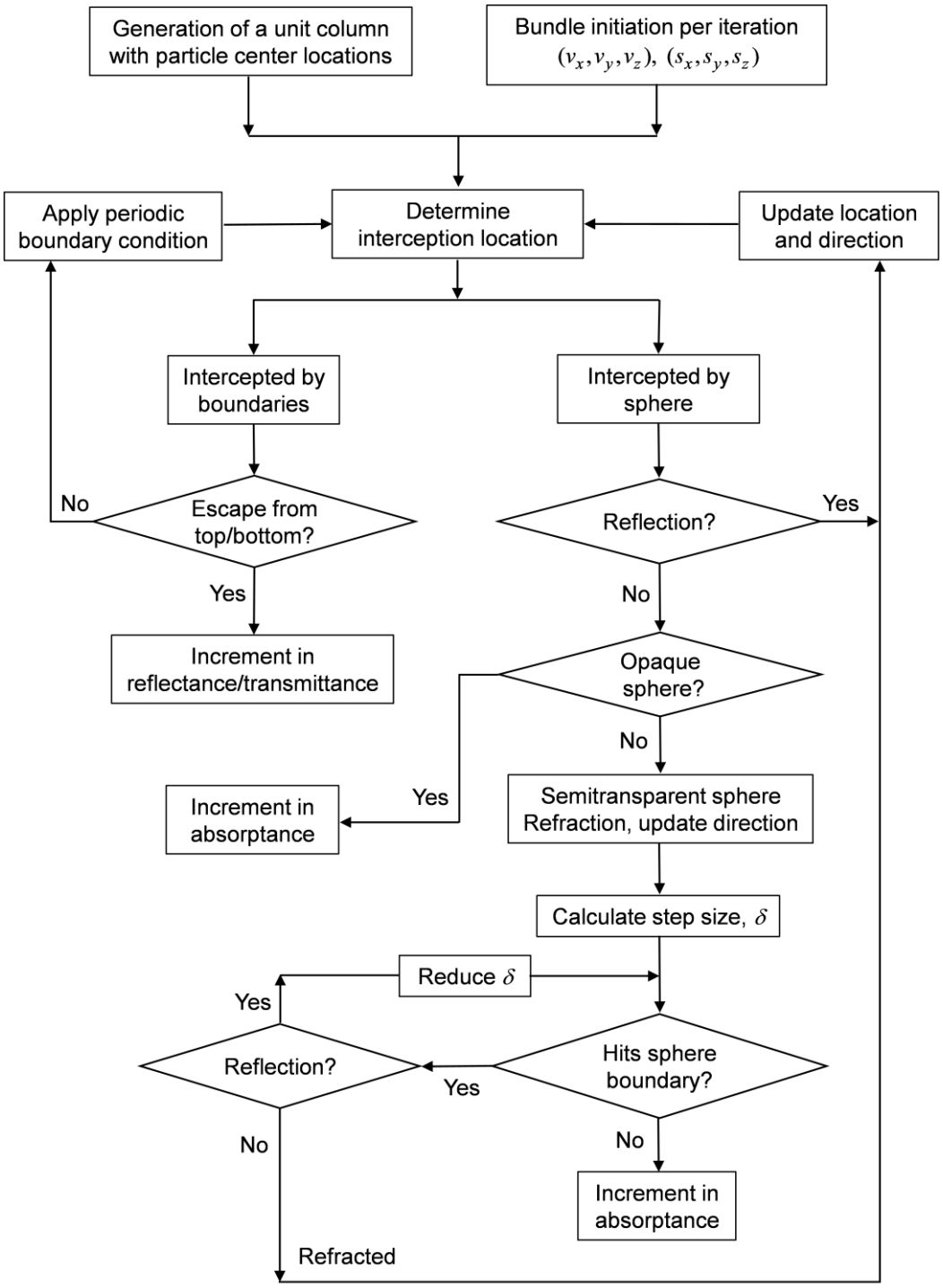

Fig. 2. Flow chart of the Monte Carlo ray-tracing simulation in a particle bed with the unit-column representation (periodic boundary condition).

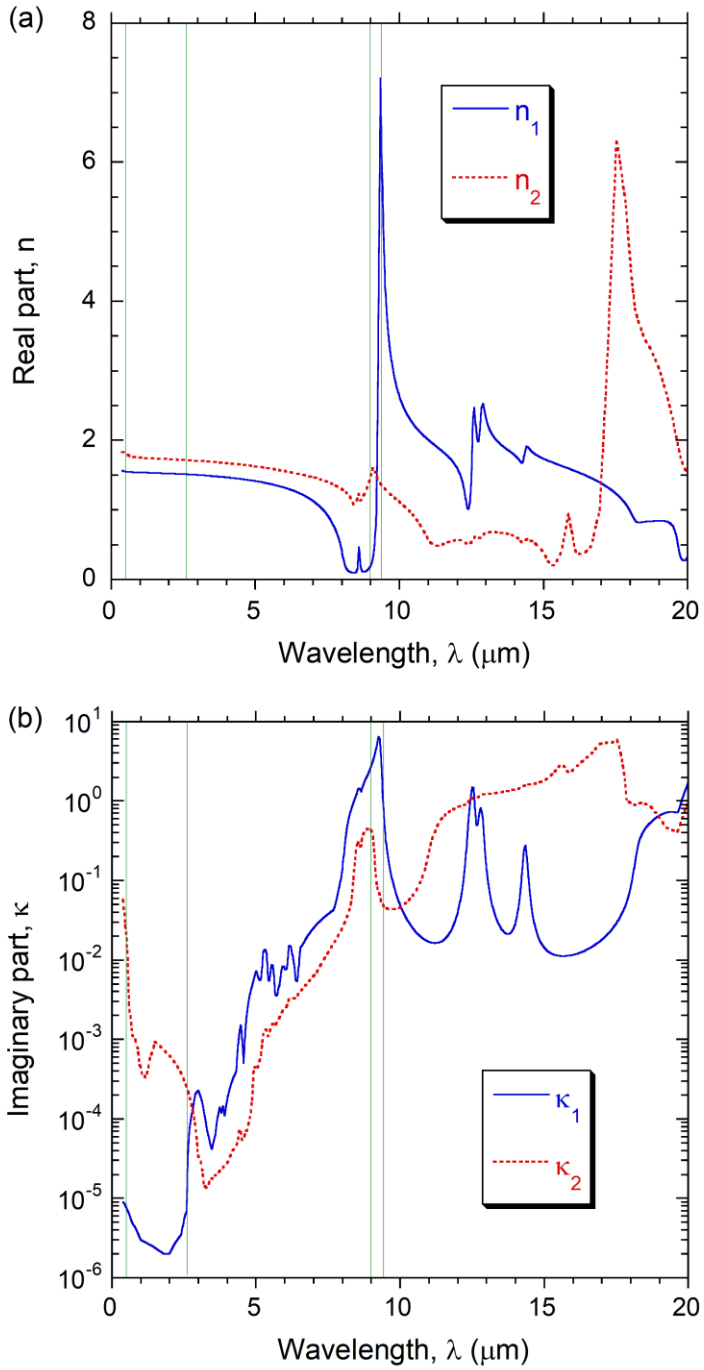

Fig. 3. Complex refractive index of silica (type 1) and bauxite (type 2): (a) real part; (b) imaginary part. The vertical lines indicate the four representative wavelengths chosen for the present study, *i.e.*, $\lambda = 0.5$, 2.6, 9.0, and 9.35 μm.

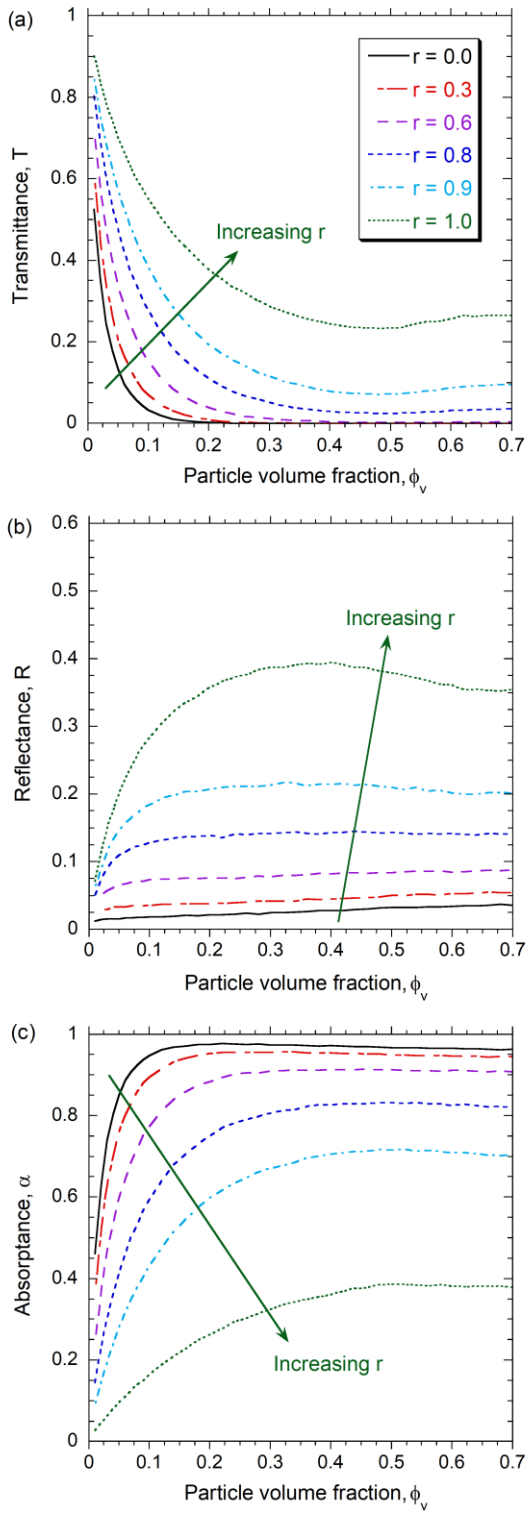

Fig. 4. Radiative properties of packed bed with bauxite and silica particles at λ = 0.5 μm obtained using the Monte Carlo simulation: (a) transmittance; (b) reflectance; (c) absorptance. The number of layers (K) is set as 15 for all simulations.

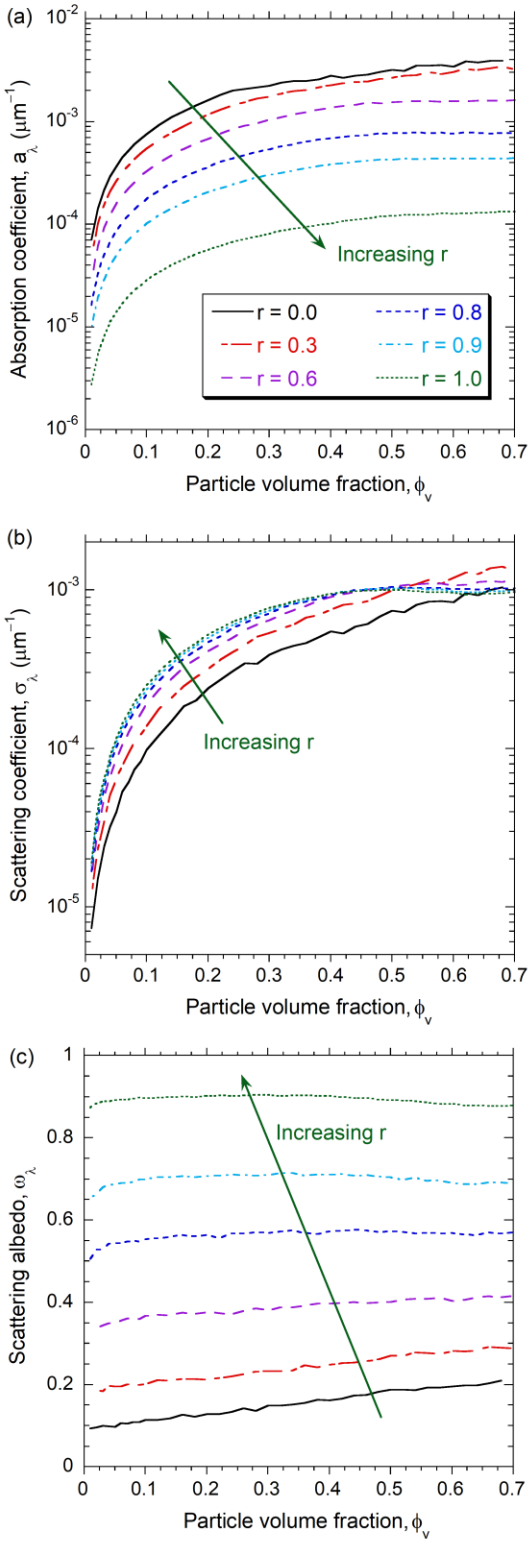

Fig. 5. IAD results for particle bed mixture at λ = 0.5 μm: (a) absorption coefficient; (b) scattering coefficient; (c) scattering albedo.

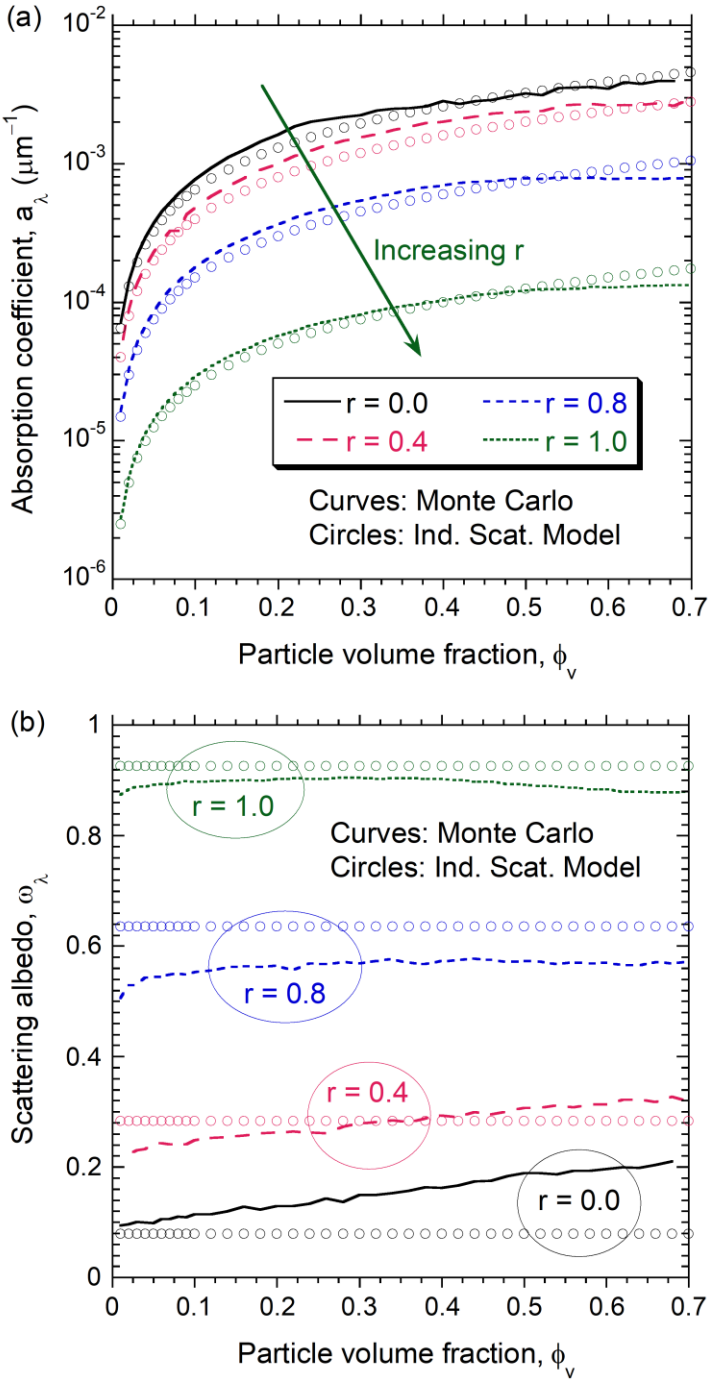

Fig. 6. Comparison of the independent scattering model with the Monte Carlo simulation for $\lambda = 0.5$ μm: (a) absorption coefficient; (b) scattering albedo.

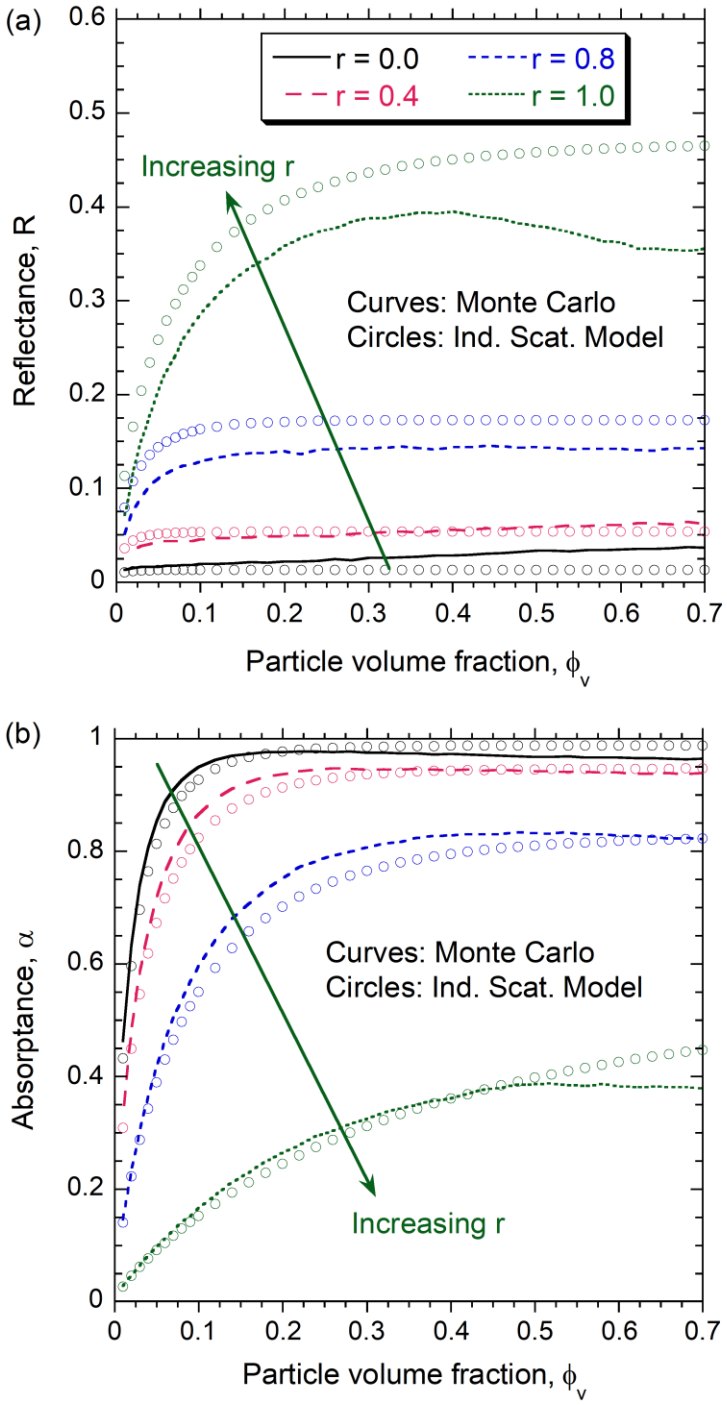

Fig. 7. Comparison of the independent scattering model with the Monte Carlo simulation for $\lambda = 0.5$ μm: (a) reflectance; (b) absorptance.

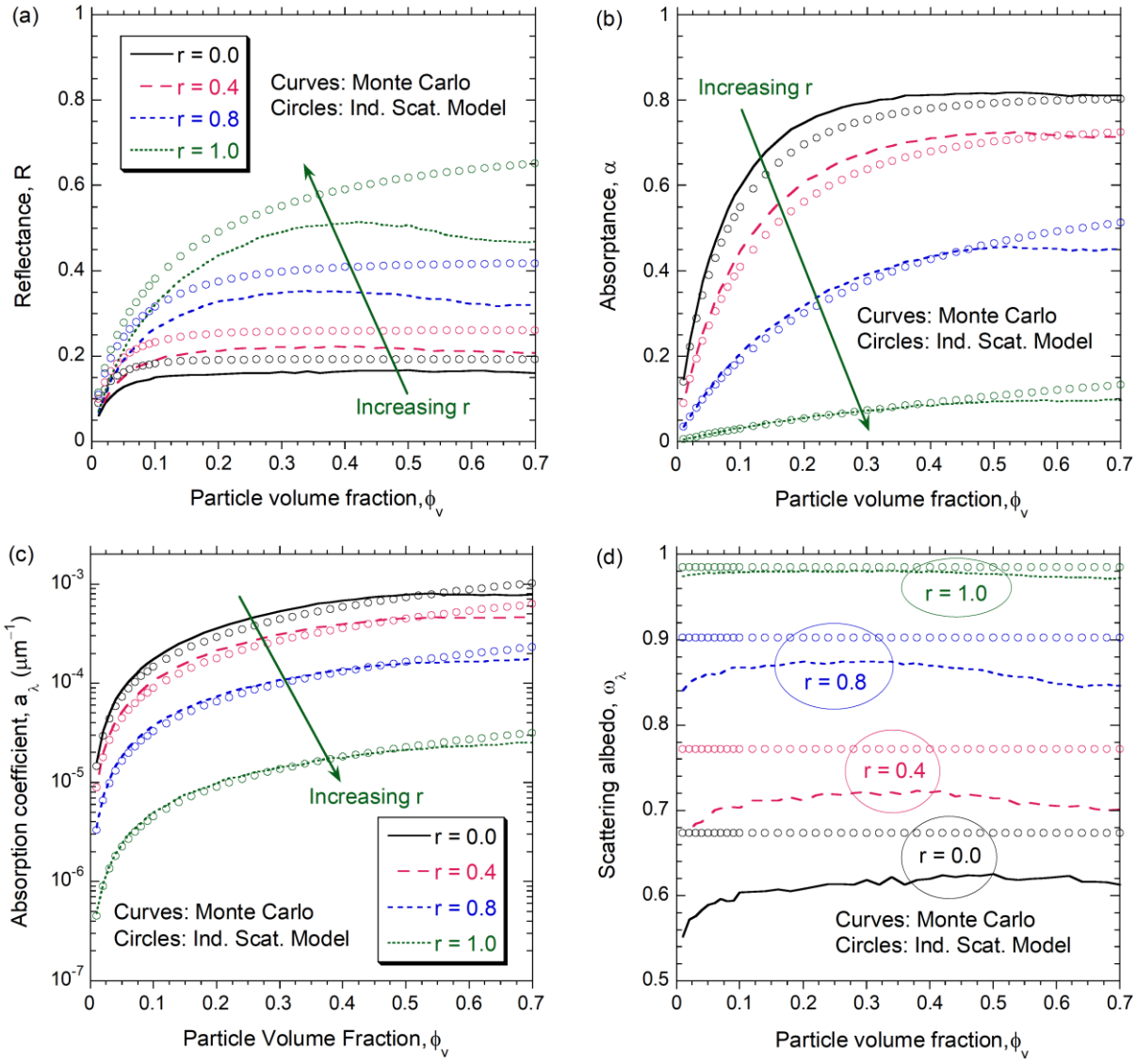

Fig. 8. Comparison of the independent scattering model with the Monte Carlo simulation for $\lambda = 2.6$ μm: (a) reflectance; (b) absorptance; (c) absorption coefficient; (d) scattering albedo.

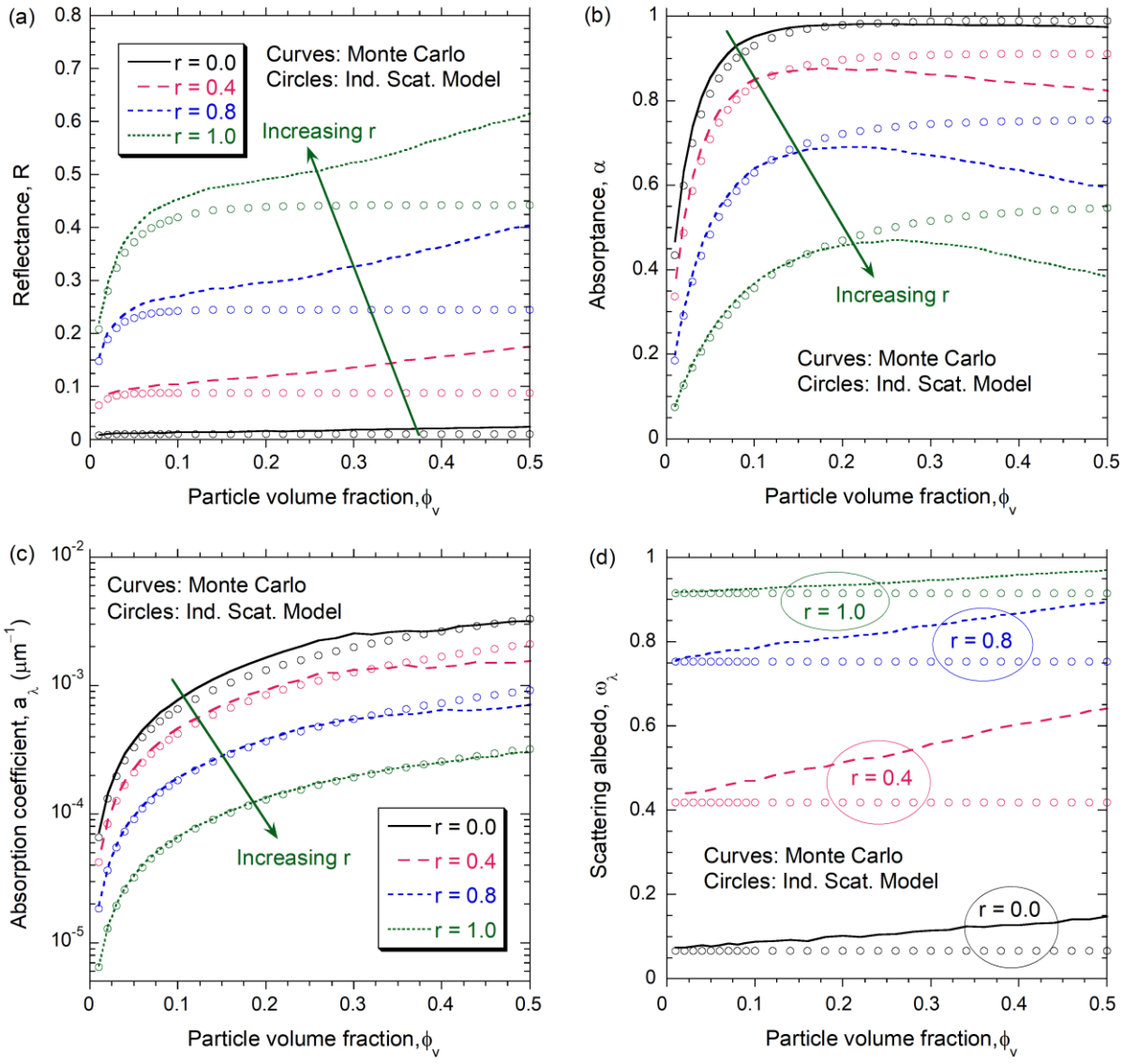

Fig. 9. Comparison of the independent scattering model with the Monte Carlo simulation for λ = 9.0 μm: (a) reflectance; (b) absorptance; (c) absorption coefficient; (d) scattering albedo.

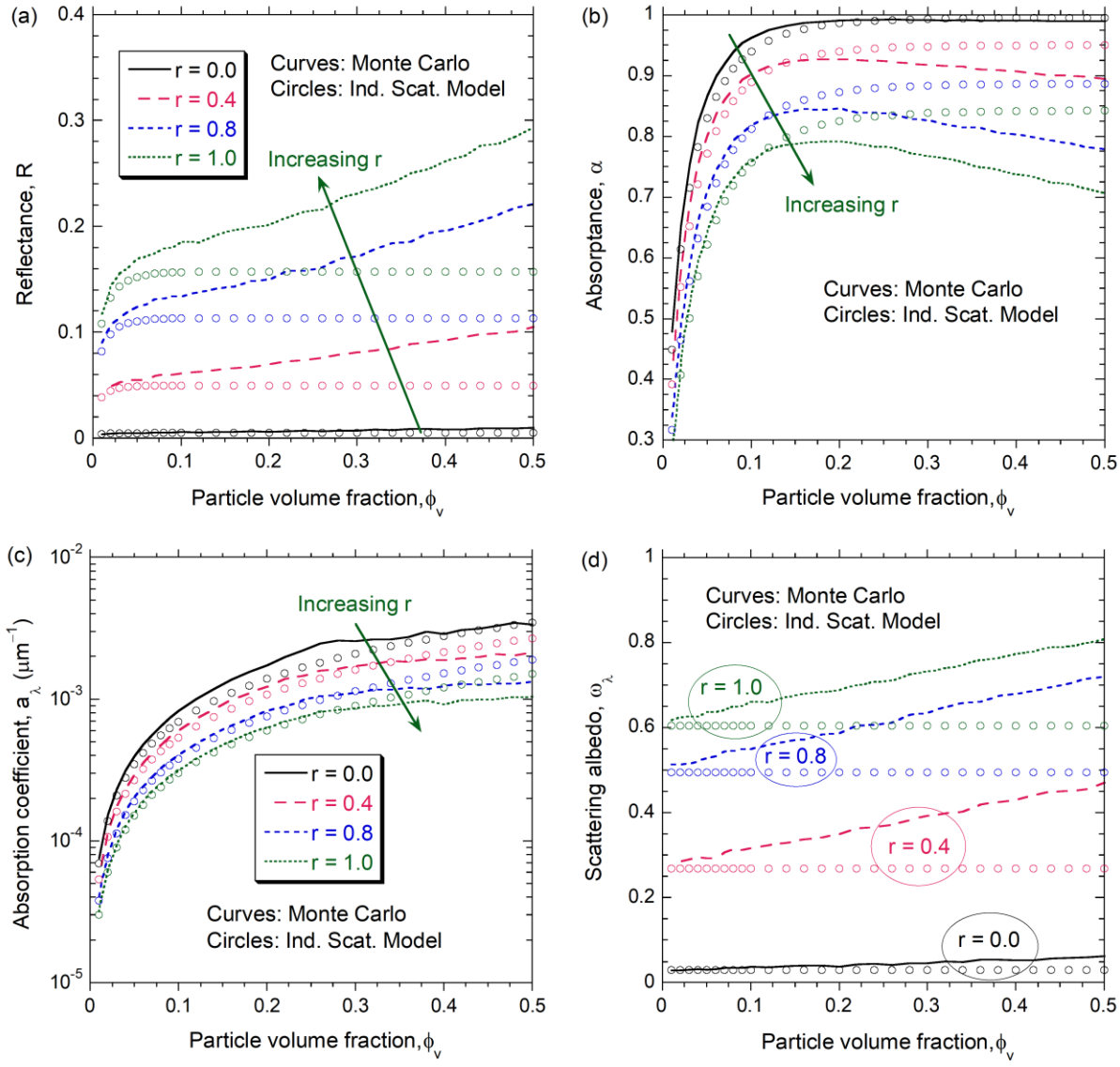

Fig. 10. Comparison of the independent scattering model with the Monte Carlo simulation for $\lambda = 9.35$ μm: (a) reflectance; (b) absorptance; (c) absorption coefficient; (d) scattering albedo.